nature communications

Article

https://doi.org/10.1038/s41467-022-33682-2

# Selective control of conductance modes in multi-terminal Josephson junctions

Received: 14 January 2022

Accepted: 29 September 2022

Published online: 08 October 2022

Check for updates

Gino V. Graziano[1,6], Mohit Gupta[1,6], Mihir Pendharkar[2,3], Jason T. Dong[4], Connor P. Dempsey[2], Chris Palmstrøm[2,4,5] & Vlad S. Pribiag[1]

The Andreev bound state spectra of multi-terminal Josephson junctions form an artificial band structure, which is predicted to host tunable topological phases under certain conditions. However, the number of conductance modes between the terminals of a multi-terminal Josephson junction must be few in order for this spectrum to be experimentally accessible. In this work, we employ a quantum point contact geometry in three-terminal Josephson devices to demonstrate independent control of conductance modes between each pair of terminals and access to the single-mode regime coexistent with the presence of superconducting coupling. These results establish a full platform on which to realize tunable Andreev bound state spectra in multi-terminal Josephson junctions.

Superconductor-semiconductor heterostructures have been studied both experimentally and theoretically over the past few decades, motivated by their potential to realize topologically protected quantum states[1–13] or gate-tunable quantum bits[14]. Such states may have applications in fault-tolerant quantum information processing[15–18]. Multi-terminal Josephson junctions (MTJJs) may provide a novel platform for realizing higher dimensional artificial band structures formed by the Andreev bound states (ABS) present in the junction. In a Josephson device with $N$ superconducting terminals, the ABS spectrum depends on the $N-1$ independent phase differences between terminals, $\phi_1, \phi_2, \ldots, \phi_{N-1}$, which act as quasimomenta, as well as on the scattering matrix $\hat{S}$ of the interstitial junction region. Furthermore, the ABS spectra of MTJJs are predicted to host topologically protected Weyl nodes and higher-order Chern numbers[19–23]. The energy gap between different ABS bands depends on the number of conductance modes between terminals, with theoretical efforts focusing on the case of unity or near-unity number of interterminal modes[19,20,24]. Approaching this condition necessitates the independent control of interterminal conductance modes in an MTJJ.

MTJJs may also find application as circuit elements for coupling multiple qubits[14,25–27]. Additionally, they have shown rich transport features such as the coexistence of superconducting and dissipative currents[28], multi-terminal fractional Shapiro steps[29,30], generalizations of multiple Andreev reflections (MAR)[31,32], multi-loop superconducting interferometry[33,34] and exotic Cooper quartet transport[35–38].

Previous experiments on MTJJs[28,32,39] have discussed the current-space differential resistance maps in three- and four-terminal devices and its dependence on parameters such as magnetic field and a single global gate voltage, but in the regime of many conductance modes. Theoretical proposals for topological ABS spectra outline the need for a small central scattering region through which the superconducting terminals are coupled in the regime of a few quantum modes, however, a global gate is not ideal for implementing this experimentally. Rather, a split-gate quantum-point-contact-like design where the junction legs can be independently depleted is necessary for the transport to be localized in a central common region (Fig. 1a).

In this work, we utilize a split-gate quantum-point contact (QPC) geometry, which allows selective gating of each leg of a Y-shaped three-terminal junction. With this approach, we demonstrate control over conductance modes between pairs of terminals, along with access to the single-mode regime in the junction, coexisting with superconductivity. This establishes a potential platform for the exploration of the tunable ABS spectra of MTJJ devices. We present detailed results from two device designs with different junction dimensions and different split-gate geometries.

---

[1]School of Physics and Astronomy, University of Minnesota, Minneapolis, MN 55455, USA. [2]Electrical and Computer Engineering, University of California Santa Barbara, Santa Barbara, CA 93106, USA. [3]Materials Science and Engineering, Stanford University, Stanford, CA 94305, USA. [4]Materials Department, University of California Santa Barbara, Santa Barbara, CA 93106, USA. [5]California NanoSystems Institute, University of California Santa Barbara, Santa Barbara, CA 93106, USA. [6]These authors contributed equally: Gino V. Graziano, Mohit Gupta. e-mail: vpribiag@umn.edu

https://doi.org/10.1038/s41467-022-33682-2

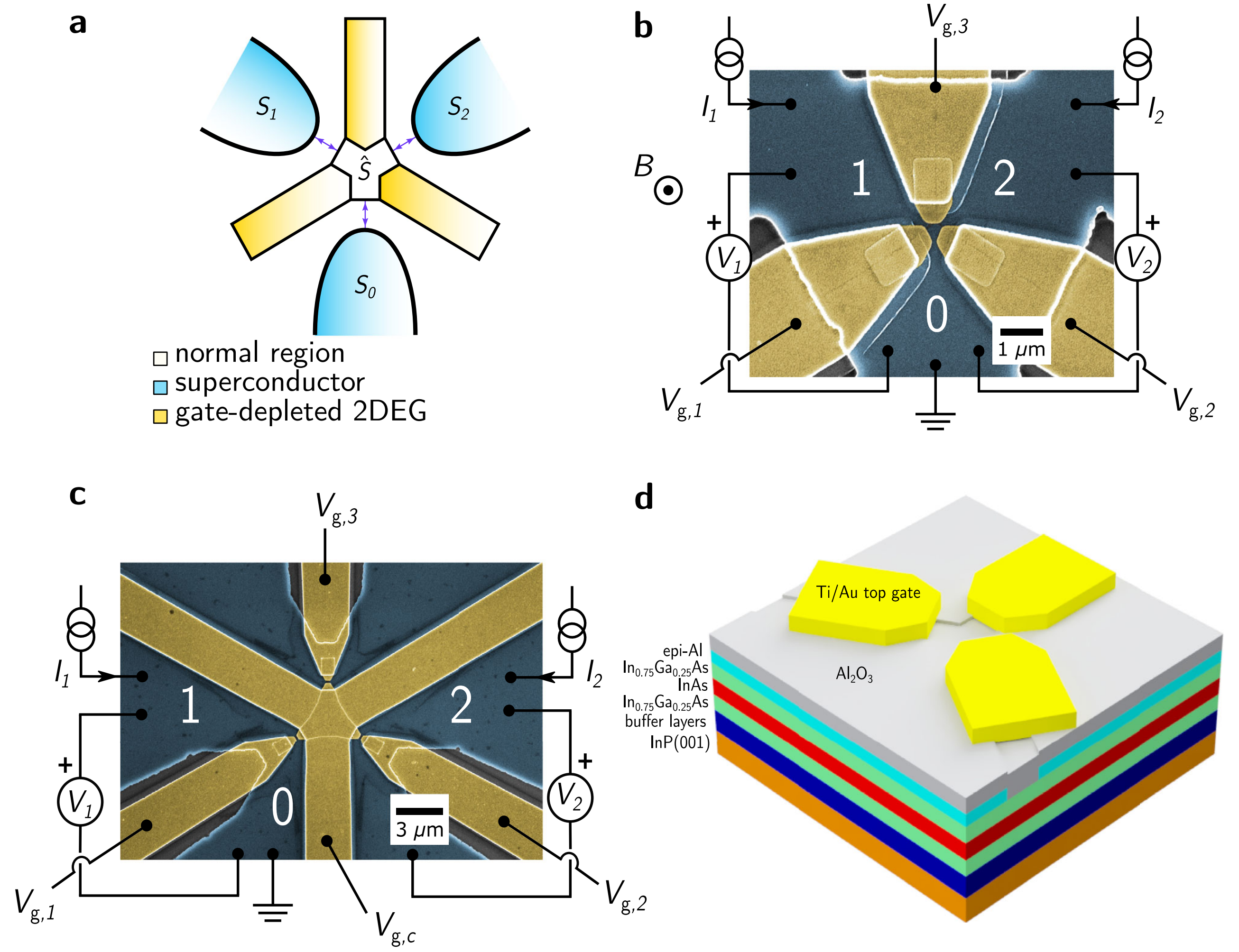

**Fig. 1 | Device geometry. a** Schematic depiction of transport in Device 1 and Device 3. The junction area under the gates, shown in yellow, can be fully depleted of carriers, leaving a central scattering region supporting a few conductance modes connected to the superconducting contacts. **b** False-color scanning electron microscope (SEM) image of Device 1, a three-terminal Josephson junction with individually tunable QPC gates, showing measurement schematic. The etched junction area is visible as the dark lines under the gates (gold-colored). **c** SEM image of Device 2, which has a central top gate that can be used both to form QPCs and to gate the central scattering area of the three-terminal junction. **d** 3D schematic of Devices 1 and 3 showing layered heterostructure.

## Results

### Device architecture

The devices are fabricated on InAs quantum well heterostructures featuring a two-dimensional electron gas (2DEG) proximitized by an epitaxial aluminum layer. High interface transparency between Al and InAs (leading to induced gap comparable to the bulk gap of Al) and coherent ballistic transport in this heterostructure have been demonstrated[6,40,41] making it an ideal platform to realize MTJJs. The heterostructure was grown on a semi-insulating InP(001) substrate using molecular-beam epitaxy. From the bottom, the heterostructure consists of a graded buffer of $In_xAl_{1-x}As$ with $x$ ranging from 0.52 to 0.81, 25 nm $In_{0.75}Ga_{0.25}As$ super-lattice, 10.72 nm $In_{0.75}Ga_{0.25}As$ bottom barrier, 4.54 nm InAs quantum well, 10.72 nm $In_{0.75}Ga_{0.25}As$ top barrier. Finally, there is a 10 nm layer of epitaxial aluminum deposited on the surface of the sample. The carrier concentration and mobility of the InAs 2DEG were measured using a Hall bar geometry and found to be $n = 1.22 \times 10^{12}\,\mathrm{cm}^{2}$ and $\mu = 9920\,\mathrm{cm}^{2}\,\mathrm{V}^{-1}\,\mathrm{s}^{-1}$ in the absence of gating (see Supplementary Fig. 1), resulting in a mean free path of $\ell \sim 180$ nm.

The Y-shaped three-terminal devices presented in this work have different junction widths and different split-gate geometries. Device 1 has a nominal contact spacing between superconducting electrodes of 50 nm, with three split gates as shown in Fig. 1b. These split gates can deplete the 2DEG underneath, forming a few-mode central region coupling each superconducting terminal. Device 2 has a nominal contact spacing of 200 nm, three split gates forming QPC-like constrictions, and also a central top gate for independent gate control of the central scattering region (Fig. 1c). Device 3 is similar in shape to Device 1, but with an electrode spacing of ~120 nm. We begin by discussing the transport properties of Device 1 and Device 2 and demonstrate the selective gate tunability of Device 2. We then show the accessibility of the single-mode regime coexistent with superconductivity in these devices.

### Transport properties

We perform DC current-bias measurements in a dilution refrigerator on all three devices using the configuration shown in Fig. 1b, c. The superconducting data for Device 1 and Device 3 were taken at fridge temperature $T \sim 40$ mK, and Device 2 at temperature $T \sim 90$ mK. We independently control the current inputs into the epitaxial aluminum terminals 1 ($I_1$) and 2 ($I_2$) while terminal 0 is grounded. We simultaneously measure the voltages of terminals

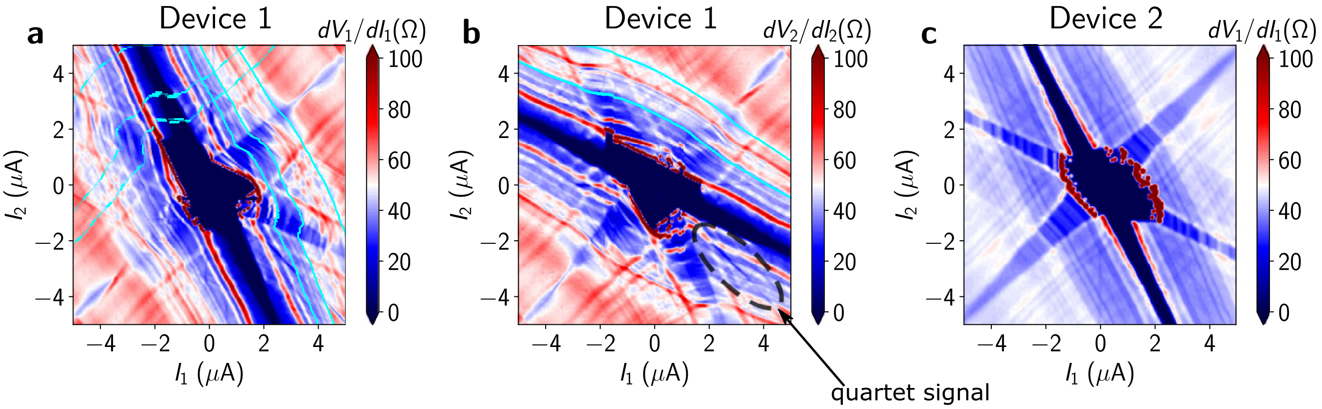

**Fig. 2 | Three-terminal differential resistance maps. a** Measurement of the differential resistance $dV_1/dI_1$ on Device 1 with a small perpendicular magnetic field. MAR along the lines $V_1 = 2\Delta/n$ are highlighted by cyan lines and along $V_1 - V_2 = 2\Delta/n$ highlighted by dashed cyan lines. **b** Measurement of $dV_2/dI_2$ on Device 1 with small perpendicular field. MAR along $V_2 = 2\Delta/n$ are shown by cyan lines. The lower resistance feature along $V_1 = -V_2$ is shown by a dashed ellipse, which can be attributed to Cooper quartet transport. Here $I_1$ is stepped and $I_2$ is swept. **c** Measurement of $dV_1/dI_1$ on Device 2 at magnetic field $B = 0$, showing MAR resonances.

1 ($V_1$) and 2 ($V_2$) relative to terminal 0. In a typical measurement, we step $I_2$ from negative to positive, and sweep $I_1$ from negative to positive at each value of $I_2$. We then calculate differential resistances $dV_1/dI_1$ and $dV_2/dI_2$ by discrete differentiation. The differential resistance maps show a central superconducting region where both $V_1$ and $V_2$ (Fig. 2a–c) are zero. Beyond this central region, superconducting arms are also observed approximately along $I_2 = -2I_1$ (Fig. 2a) where only $V_1$ is zero, and $I_1 = -2I_2$ (Fig. 2b) where only $V_2$ is zero. A third superconducting arm is observed approximately along $I_1 = I_2$. This feature is due to super-current being present between terminals 1 and 2 (Fig. 2a–c), while the other two arms have a nonzero resistance. The slopes of these superconducting arms in the $I_1, I_2$-plane can be understood by a resistor network model (see Supplementary Information).

The differential resistance maps exhibit rich MAR patterns. We can observe MAR as features of lower resistance along the lines $V_1 = 2\Delta/n$ and $V_1 - V_2 = 2\Delta/n$, where $n$ is an integer and $\Delta \sim 145\mu$V is the induced superconducting gap (estimated by fitting MAR at $V_1 = 2\Delta$). Figure 2a shows these MAR lines highlighted in cyan for $n = 2, 4, 6$. In Fig. 2b we highlight MAR along $V_2 = 2\Delta/n$ for $n = 2, 4$ in the differential resistance $dV_2/dI_2$. These three sets of MAR signatures can be understood as independent Andreev reflections between all three pairs of terminals. We also observe a signature of Cooper quartet transport[35–38,42], indicated by a lower resistance feature along the line $V_1 = -V_2$. The differential resistance maps can also be plotted as a function of $V_1$, $V_2$ where the quartet signature is clearly visible along the $V_1 = -V_2$ diagonal (see Supplementary Fig. 2). This places Device 1 in the phase-coherent quasiballistic regime and opens up interesting possibilities for investigating cross-terminal quantum correlations.

These features are also observed for Device 2 as shown in Fig. 2c, despite the junction width being nearly four times larger. This is possible due to the highly transparent interface between the epitaxial aluminum and InAs quantum well of the heterostructure, and displays the robustness of our fabrication process for MTJJs and the high degree of reproducibility. The central superconducting region is not current-symmetric in the differential resistance maps for Device 1. This indicates the presence of a small residual magnetic field resulting in asymmetric critical current[32,43], as verified in Device 2 by correcting for this residual field in our external superconducting magnet. We can observe the disappearance of this asymmetry when the perpendicular magnetic field, $B$, vanishes, as shown in Fig. 2c.

## Selective control of conductance in three-terminal Josephson junctions

A distinctive feature of these devices is their independent split top gates, enabling individual control of each leg of the Y-shaped junction. In order to demonstrate local control of the Josephson junctions formed between each pair of terminals, we can examine the results of gate-depleting carriers in each of the legs selectively. Negative voltage gating of a leg results in narrowing of the width of the superconducting arm associated with it in the differential resistance map. Additionally, the slopes of the lines change in the $I_1$,$I_2$-plane about which superconducting features are centered. These slope changes are due to an increase in the normal state resistance ($R_n$) of the leg, which affects the division of dissipative currents between the three terminals. When the normal state resistances in the resistor network are $R_{n,1}$, $R_{n,2}$, $R_{n,3}$, the feature due to super-current between terminals 1 and 0 ($V_1 = 0$) falls along the line $I_2 = -\left(R_{n,3}/R_{n,2} + 1\right)I_1$. For super-current between terminals 2 and 0 ($V_2 = 0$), this relation is $I_2 = -\left(R_{n,3}/R_{n,1} + 1\right)^{-1}I_1$ and between terminals 1 and 2 ($V_1 - V_2 = 0$) it lies along $I_2 = (R_{n,1}/R_{n,2})I_1$. Thus, we can demonstrate truly selective gating in our devices by examining the narrowing of superconducting features and their modified slopes.

As a starting point, we measure the differential resistance $dV_1/dI_1$ with the same applied voltage on all four independent gates in Device 2 (three gates on the legs and one central gate) with $V_g = -5$ V (Fig. 3a). This voltage is applied to amplify the effect of selective gating, since the superconducting features become more sensitive to gating at sufficiently negative gate voltages. Although the applied voltage is the same, we can see a minor asymmetry of features compared to the plot at the zero gate (Fig. 2c). We then decrease the voltage further only on the gate between terminals 1 and 2 ($V_{g,3}$) (Fig. 3b). This results in a distinct change in the differential resistance map as can be seen in Fig. 3c. The superconducting arm due to supercurrent between terminals 1 and 2 ($V_1 - V_2 = 0$) dramatically decreases in width. The slope of the superconducting arm where $V_1 = 0$ has tilted toward the line $I_1 = 0$, and the $V_2 = 0$ superconducting arms has tilted toward the line $I_2 = 0$. The slope of the narrowing arm ($V_1 - V_2 = 0$) has remained unchanged. This is consistent with the limiting cases of the equations in the previous paragraph for $R_{n,3} \gg R_{n,1}, R_{n,2}$. We have studied the effect of selective gating on the other two legs as well, and the slope changes were found to be consistent with this resistor network model (see Supplementary Information).

Additionally, we performed simulations of the system using a three-terminal resistively and capacitively shunted junction (RCSJ)

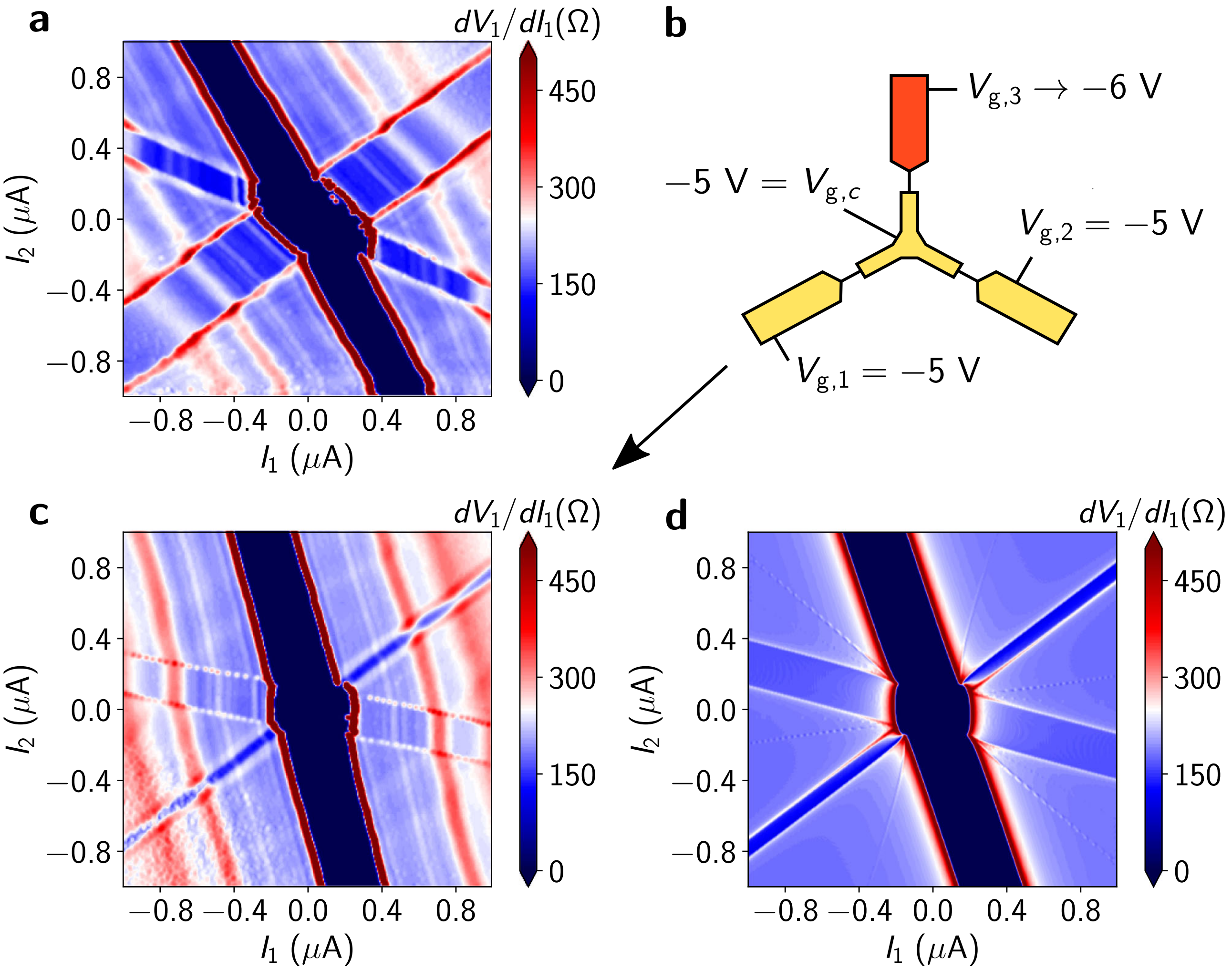

**Fig. 3 | Selective gating.** **a** Measurement of $dV_1/dI_1$ on Device 2, $B = 0$, $T \sim 90$ mK with $V_{g,c}$, $V_{g,1}$, $V_{g,2}$, $V_{g,3} = -5$ V. **b** Schematic of gate configuration for the selective gating of the junction leg between terminals 1 and 2. **c** Measurement of $dV_1/dI_1$ at $V_{g,c}$, $V_{g,1}$, $V_{g,2} = -5$ V and $V_{g,2} = -6$ V. **d** RCSJ simulation of $dV_1/dI_1$ with parameters tuned to reproduce the features of experimental data.

network model by solving coupled differential equations obtained by a multi-terminal generalization of the RCSJ model[30]. Details of the simulation and model parameters can be found in the Supplementary information. This network model consists of three nodes with RCSJs between each of them, and thus contains nine independent parameters, namely the critical currents $I_{c,i}$, normal state resistances $R_{n,i}$ and capacitances $C_i$. The effect of gating was modeled by increasing the normal state resistance as well as decreasing the critical current of the RCSJ between two nodes relative to the others. Tuning the resistance and critical current parameters allows us to precisely reproduce the features seen in current-biased differential resistance data for preferential gating along each of the three legs (Fig. 3d). The striped MAR features are not reproduced, as this is a quantum phenomenon not captured by the semiclassical RCSJ model. This conclusively shows independent control of conductance modes in each leg of the MTJJ.

## Few-mode three-terminal josephson junction

To demonstrate tunability of conductance modes in our devices, we perform DC voltage-biased measurements on Device 1. We apply a DC source-drain voltage bias $V_{sd}$ between a pair of terminals, with the third terminal electrically floating, and measure the resultant DC current $I_{meas}$. The voltage drop across the device $V_{meas}$ is also monitored simultaneously to exclude the effect of series resistance. We can then compute the differential resistance $dV_{meas}/dI_{meas}$ and differential conductance $G = dI_{meas}/dV_{meas}$ by discrete differentiation.

Figure 4a shows a map of differential resistance between terminals 1 and 2 in Device 1 as a function of $V_{sd}$ and gate voltage applied to all three split gates, $V_g$. The critical current countours are observed as areas of zero resistance, and MAR is observed as areas of reduced resistance for $V_{sd} \lesssim 2$ mV. These features show periodic oscillations as a function of gate voltage. These oscillations indicate Fabry-Pérot interference, which has been observed before in a two-terminal graphene Josephson junction[44]. This results from the interference of supercurrent trajectories that travel ballistically from one contact to the other, conclusively showing ballistic transport between the two terminals. Supercurrent is present between the two measured terminals at the conductance values ~1.0 $G_0$, where $G_0 = 2e^2/h$ is the conductance quantum. We also observe conductance plateaus as a function of $V_g$ (Fig. 4b). The step height of these plateaus differs from the conductance quantum $G_0$, and the quantization weakens for higher values of conductance. This is likely due to the effect of finite source-drain bias on the conductance. At finite bias, the value of the conductance steps is determined by the number of quasi-1D subbands falling within the bias window set by $V_{sd}$[41,45,46]. Such finite-bias conductance measurements are necessary due to the presence of superconductivity and MAR resonances below $V_{meas} < 2\Delta$[46–48].

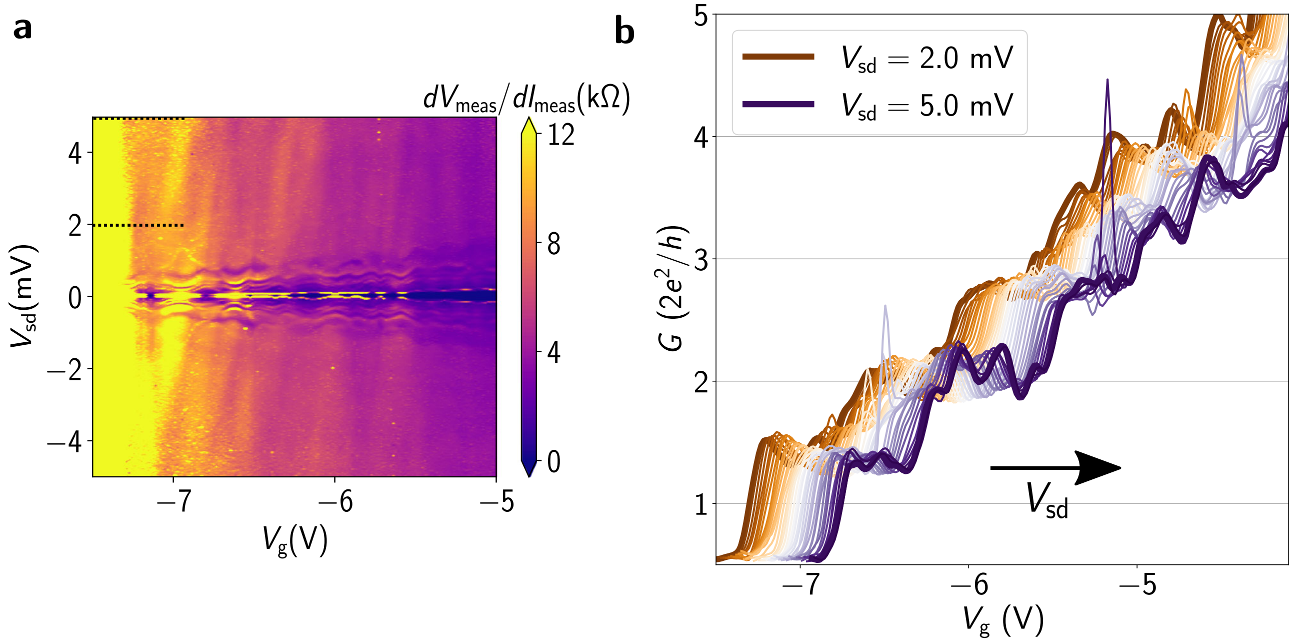

**Fig. 4 | Single-mode MTJJ. a** Differential conductance as a function of source-drain bias $V_{\mathrm{sd}}$ and gate voltage $V_{\mathrm{g}}$ for terminal pair 1 and 2 for Device 1 at $B = 0$ and $T \sim 40$ mK. **b** Differential conductance as a function of gate voltage for different $V_{\mathrm{sd}}$ for Device 1 at $B = 0$ and $T \sim 40$ mK. The curves correspond to $V_{\mathrm{sd}}$ values between 2.0 mV and 5.0 mV (shown by dashed black lines in **a** in increments of 0.125 mV, and are each offset along the $V_{\mathrm{g}}$ axis (arrow indicating direction of increasing $V_{\mathrm{sd}}$) by 3 mV for clarity.

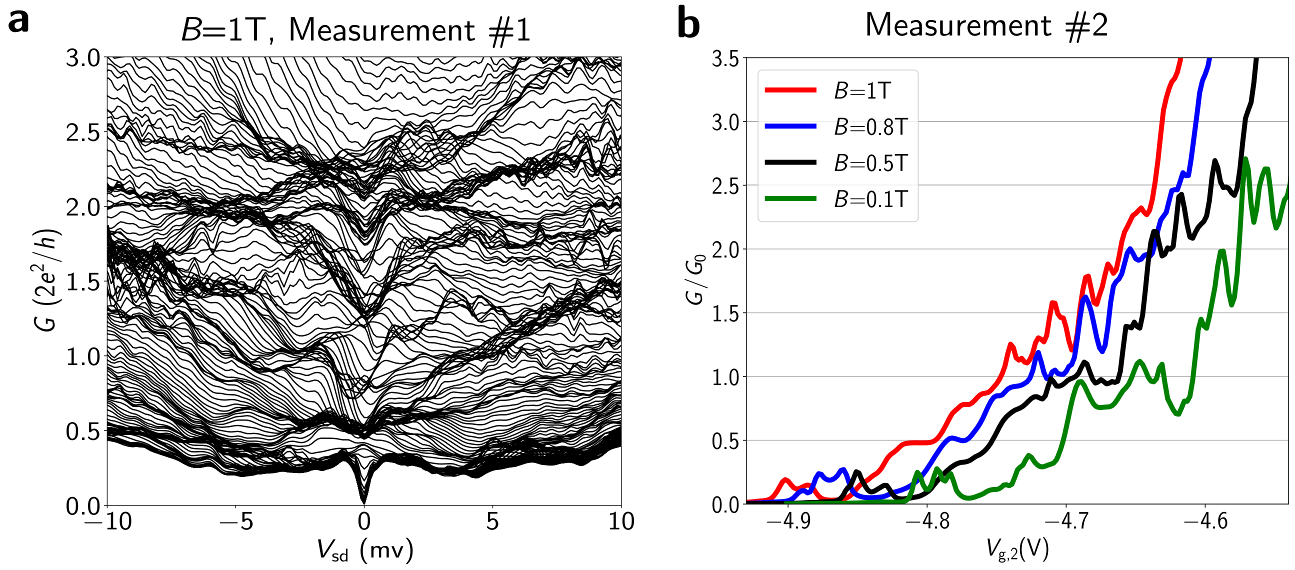

**Fig. 5 | Zero-bias conductance measurements. a** Waterfall plot of differential conductance as a function of $V_{\mathrm{sd}}$ for a range of gate voltages from $V_{\mathrm{g},2} = -5.26$ V to $V_{\mathrm{g},2} = -5.5$ V with a step size $\delta V_{\mathrm{g}} = 1.3$ mV, for Device 3. **b** Zero-bias differential conductance for Device 3 for different values of out-of-plane magnetic field. For these measurements we have set $V_{\mathrm{g},1} = -6$ V and $V_{\mathrm{g},3} = -3$ V. The curves are offset on the gate voltage axis by 0.02 V, 0.06 V and 0.1 V for $B = 0.8$ T, $B = 0.5$ T, and $B = 0.1$ T, respectively for clarity. All measurements were taken at $T = 40$ mK.

To measure conductance at zero-bias, an out-of-plane magnetic field can be applied to eliminate superconducting effects. We measure Device 3 (lithographically identical to Device 1) in this regime. Conductance measurements are performed for terminal pair 2 and 0 using standard lock-in techniques. The waterfall plot of conductance in Fig. 5a shows the bunching of lines at zero-bias at values of ~0.5, 1, 1.5, and 2.0 $G_0$ due to spin splitting of the subbands. At finite bias, the waterfall plot shows bunching of curves at conductance values between integer multiples of $e^2/h$ as previously observed in two-terminal superconducting QPCs with magnetic field[46]. This can cause the step heights to differ from the conductance quantum $G_0$, as observed for Device 1 at $B = 0$ T. In a separate measurement, conductance scans are performed by varying the magnetic field and keeping $V_{\mathrm{sd}} = 0$ V. As shown in the red curve in Fig. 5b, conductance steps are observed near the conductance values where lines bunch at $B = 1$ T. Fig. 5b further shows that the plateaus become more well-defined as $B$ is increased. Additionally, resonances in the conductance data are smoothed by application of magnetic field, attributed to the suppression of coherent backscattering due to the Aharanov-Bohm phase contribution. Conductance measurements at $B = 0$ T are also performed for all three pairs of the terminals and are consistent with those on Device 1 (Supplementary Fig. 5). The voltage range $V_{g,2}$ is different between Fig. 5a, b due to gate hysteresis.

This demonstrates that transport between the two measured terminals takes place via a few conductance modes. Only the first few modes are individually resolved by our measurements, which could be due to a non-ideal potential profile in the central region of the junction, where the confining potential may be weakened due to screening by the Al contacts. However, to resolve the ABS spectra of MTJJs only the first few conductance modes are necessary[19,26]. Moreover, theory predicts that the quantized transconductance signatures of Weyl nodes can only be resolved in the single-mode limit[24].

Similar data are obtained for all three pairs of terminals for Device 2 as well (Supplementary Fig. 6), and the single-mode regime is accessible, coexistent with superconductivity. However, the conductance quantization is less robust than that seen in Devices 1 and 3 (Supplementary Fig. 6). This can be attributed to the mean free path in the InAs QW ($\ell \sim 180$ nm) being comparable to the junction width of 200 nm, increasing the susceptibility to scattering relative to Devices 1 and 3. It should be noted that the maximum measured resistance saturates at ~100 kΩ for Device 1 and ~10 kΩ for Device 2. For the Device 3 data in Fig. 5, we subtract this conductance contribution (~40 kΩ) at each value of the magnetic field. These residual resistances can be attributed to trivial edge modes of InAs present in the etched mesa. These surface modes do not respond to a top gate and are difficult to eliminate in InAs[49–52], but not expected to be detrimental to the investigation of the ABS.

## Discussion

We demonstrate phase-coherent quasiballistic transport in three-terminal split-gated Josephson devices, with access to the single-quantum-mode regime independently in each leg. This is the first demonstration of the accessibility of all theoretical constraints necessary to observe topologically protected states formed in ABS of MTJJs. This presents a promising alternative platform to realize topological quantum states, complementary to the much-explored Majorana zero modes. Realization of topologically protected states in the ABS spectra of MTJJs also requires fine-tuning of the scattering matrix of the central region, which can in principle be achieved with geometries similar to that of Device 2. Devices with more than three terminals can be explored on the same material platform with a similar gate structure, making detection of these exotic states more likely using a range of proposed approaches.

## Methods

### Device fabrication

Standard electron-beam lithography (EBL) and wet etching techniques were used to fabricate a mesa and the Y-shaped junction area. Approximately 40 nm of $Al_2O_3$ dielectric was deposited using thermal atomic layer deposition. Using EBL, split gates are defined over the junction area and electrodes are deposited using electron-beam evaporation of Ti/Au (5 nm/25 nm). In separate lithography step thicker gold contacts (Ti/Au, 5 nm/200 nm) are made to the gate electrodes[53].

### Measurement details

Differential resistance maps on both devices and conductance quantization data on Device 1 were obtained by low-noise DC transport measurements in a $^3$He/$^4$He dilution refrigerator. For the conductance quantization data on Device 2 (in Supplementary Material), standard low-frequency lock-in techniques were used with a small excitation voltage and a frequency of 19 Hz. For the AC conductance measurements, the raw data are corrected by subtracting the series filter and the ammeter resistances which combine to give 6.6 kΩ. Low-pass Gaussian filtering was used to smooth numerical derivatives.

## Data availability

Source data for the figures presented in this paper are available in the following Zenodo database [https://zenodo.org/record/6718253].

## Code availability

The data plotting code and code for the performed simulations are available in the following Zenodo database [https://zenodo.org/record/6718253].

## References

1. Doh, Y.-J. et al. Tunable supercurrent through semiconductor nanowires. *Science* **309**, 272–5 (2005).
2. Williams, J. R. et al. Unconventional josephson effect in hybrid superconductor-topological insulator devices. *Phys. Rev. Lett.* **109**, 056803 (2012).
3. Günel, H. Y. et al. Supercurrent in Nb/InAs-nanowire/Nb Josephson junctions. *J. Appl. Phys.* **112**, 034316 (2012).
4. Hart, S. et al. Induced superconductivity in the quantum spin Hall edge. *Nat. Phys.* **10**, 638–643 (2014).
5. Pribiag, V. S. et al. Edge-mode superconductivity in a two-dimensional topological insulator. *Nat. Nanotechnol.* **10**, 593–597 (2015).
6. Kjaergaard, M. et al. Transparent semiconductor-superconductor interface and induced gap in an epitaxial heterostructure josephson junction. *Phys. Rev. Appl.* **7**, 034029 (2017).
7. Deacon, R. S. et al. Josephson radiation from gapless andreev bound states in HgTe-based topological junctions. *Phys. Rev. X* **7**, 021011 (2017).
8. Suominen, H. J. et al. Zero-energy modes from coalescing andreev states in a two-dimensional semiconductor-superconductor hybrid platform. *Phys. Rev. Lett.* **119**, 176805 (2017).
9. Lutchyn, R. M. et al. Majorana zero modes in superconductor-semiconductor heterostructures. *Nat. Rev. Mater.* **3**, 52–68 (2018).
10. Ghatak, S. et al. Anomalous fraunhofer patterns in gated josephson junctions based on the bulk-insulating topological insulator BiSbTe$Se_2$. *Nano Lett.* **18**, 5124–5131 (2018).
11. Laroche, D. et al. Observation of the 4$\pi$-periodic Josephson effect in indium arsenide nanowires. *Nat. Commun.* **10**, 245 (2019).
12. Fornieri, A. et al. Evidence of topological superconductivity in planar Josephson junctions. *Nature* **569**, 89–92 (2019).
13. Ren, H. et al. Topological superconductivity in a phase-controlled Josephson junction. *Nature* **569**, 93–98 (2019).
14. Casparis, L. et al. Superconducting gatemon qubit based on a proximitized two-dimensional electron gas. *Nat. Nanotechnol.* **13**, 915–919 (2018).
15. Kitaev, A. Y. Unpaired Majorana fermions in quantum wires. *Phys. -Uspekhi* **44**, 131–136 (2001).
16. Kitaev, A. Y. Fault-tolerant quantum computation by anyons. *Ann. Phys.* **303**, 2–30 (2003).
17. Nayak, C., Simon, S. H., Stern, A., Freedman, M. & Das Sarma, S. Non-Abelian anyons and topological quantum computation. *Rev. Mod. Phys.* **80**, 1083–1159 (2008).
18. Sarma, S. D., Freedman, M. & Nayak, C. Majorana zero modes and topological quantum computation. *npj Quantum Inf.* **1**, 15001 (2015).
19. Riwar, R. P., Houzet, M., Meyer, J. S. & Nazarov, Y. V. Multi-terminal Josephson junctions as topological matter. *Nat. Commun.* **7**, 11167 (2016).
20. Meyer, J. S. & Houzet, M. Nontrivial chern numbers in three-terminal josephson junctions. *Phys. Rev. Lett.* **119**, 136807 (2017).
21. Xie, H. Y., Vavilov, M. G. & Levchenko, A. Topological Andreev bands in three-terminal Josephson junctions. *Phys. Rev. B* **96**, 161406(R) (2017).

22. Xie, H. Y., Vavilov, M. G. & Levchenko, A. Weyl nodes in Andreev spectra of multiterminal Josephson junctions: chern numbers, conductances, and supercurrents. *Phys. Rev. B* **97**, 035443 (2018).
23. Xie, H.-Y., Hasan, J. & Levchenko, A. Non-abelian monopoles in the multiterminal josephson effect. *Phys. Rev. B* **105**, L241404 (2022).
24. Eriksson, E., Riwar, R.-P., Houzet, M., Meyer, J. S. & Nazarov, Y. V. Topological transconductance quantization in a four-terminal josephson junction. *Phys. Rev. B* **95**, 075417 (2017).
25. van Heck, B., Akhmerov, A. R., Hassler, F., Burrello, M. & Beenakker, C. W. J. Coulomb-assisted braiding of majorana fermions in a josephson junction array. *N. J. Phys.* **14**, 035019 (2012).
26. van Heck, B., Mi, S. & Akhmerov, A. R. Single fermion manipulation via superconducting phase differences in multiterminal josephson junctions. *Phys. Rev. B* **90**, 155450 (2014).
27. Qi, Z. et al. Controlled-Z gate for transmon qubits coupled by semiconductor junctions. *Phys. Rev. B* **97**, 134518 (2018).
28. Draelos, A. W. et al. Supercurrent flow in multiterminal graphene josephson junctions. *Nano Lett.* **19**, 1039–1043 (2019).
29. Deb, O., Sengupta, K. & Sen, D. Josephson junctions of multiple superconducting wires. *Phys. Rev. B* **97**, 174518 (2018).
30. Arnault, E. G. et al. Multiterminal inverse ac josephson effect. *Nano Lett.* **21**, 9668–9674 (2021).
31. Nowak, M. P., Wimmer, M. & Akhmerov, A. R. Supercurrent carried by nonequilibrium quasiparticles in a multiterminal Josephson junction. *Phys. Rev. B* **99**, 075416 (2019).
32. Pankratova, N. et al. Multiterminal josephson effect. *Phys. Rev. X* **10**, 031051 (2020).
33. Strambini, E. et al. The ω-SQUIPT: phase-engineering of Josephson topological materials. *Nat. Nanotechnol.* **11**, 1055–1059 (2016).
34. Vischi, F. et al. Coherent transport properties of a three-terminal hybrid superconducting interferometer. *Phys. Rev. B* **95**, 054504 (2017).
35. Freyn, A., Douçot, B., Feinberg, D. & Mélin, R. Production of nonlocal quartets and phase-sensitive entanglement in a superconducting beam splitter. *Phys. Rev. Lett.* **106**, 257005 (2011).
36. Pfeffer, A. H. et al. Subgap structure in the conductance of a three-terminal Josephson junction. *Phys. Rev. B* **90**, 075401 (2014).
37. Cohen, Y. et al. Nonlocal supercurrent of quartets in a three-terminal Josephson junction. *Proc. Natl Acad. Sci. USA* **115**, 6991–6994 (2018).
38. Huang, K.-F. et al. Evidence for 4e charge of cooper quartets in a biased multi-terminal graphene-based josephson junction. *Nat. Commun.* **13**, 3032 (2022).
39. Graziano, G. V., Lee, J. S., Pendharkar, M., Palmstrøm, C. J. & Pribiag, V. S. Transport studies in a gate-tunable three-terminal josephson junction. *Phys. Rev. B* **101**, 054510 (2020).
40. Shabani, J. et al. Two-dimensional epitaxial superconductor-semiconductor heterostructures: a platform for topological superconducting networks. *Phys. Rev. B* **93**, 155402 (2016).
41. Lee, J. S. et al. Transport studies of Epi-Al/InAs two-dimensional electron gas systems for required building-blocks in topological superconductor networks. *Nano Lett.* **19**, 3083 (2019).
42. Arnault, E. G. et al. Dynamical stabilization of multiplet supercurrents in multiterminal Josephson junctions. *Nano Lett.* **22**, 7073–7079 (2022).
43. Gupta, M. et al. Superconducting diode effect in a three-terminal Josephson device, https://arxiv.org/abs/2206.08471 (2022).
44. Calado, V. E. et al. Ballistic josephson junctions in edge-contacted graphene. *Nat. Nanotechnol.* **10**, 761–764 (2015).
45. Patel, N. K. et al. Evolution of half plateaus as a function of electric field in a ballistic quasi-one-dimensional constriction. *Phys. Rev. B* **44**, 13549–13555 (1991).
46. Gallagher, P., Lee, M., Williams, J. R. & Goldhaber-Gordon, D. Gate-tunable superconducting weak link and quantum point contact spectroscopy on a strontium titanate surface. *Nat. Phys.* **10**, 748–752 (2014).
47. Thierschmann, H. et al. Transport regimes of a split gate superconducting quantum point contact in the two-dimensional $LaAlO_3$/$SrTiO_3$ superfluid. *Nat. Commun.* **9**, 2276 (2018).
48. Mikheev, E., Rosen, I. T. & Goldhaber-Gordon, D. Quantized critical supercurrent in $SrTiO_3$-based quantum point contacts. *Sci. Adv.* **7**, eabi6520 (2021).
49. Noguchi, M., Hirakawa, K. & Ikoma, T. Intrinsic electron accumulation layers on reconstructed clean inas(100) surfaces. *Phys. Rev. Lett.* **66**, 2243–2246 (1991).
50. Olsson, L. O. et al. Charge accumulation at inas surfaces. *Phys. Rev. Lett.* **76**, 3626–3629 (1996).
51. Mueller, S. et al. Edge transport in inas and inas/gasb quantum wells. *Phys. Rev. B* **96**, 075406 (2017).
52. Mittag, C. et al. Passivation of edge states in etched inas sidewalls. *Appl. Phys. Lett.* **111**, 082101 (2017).
53. Lee, J. S. et al. Contribution of top barrier materials to high mobility in near-surface InAs quantum wells grown on GaSb(001). *Phys. Rev. Mater.* **3**, 014603 (2019).

## Acknowledgements

We thank Alex Levchenko and Steven Koester for their helpful discussions. This work was supported primarily by the National Science Foundation under Award No. DMR-1554609. The work at UCSB was supported by the Department of Energy under Award No. DE-SC0019274. The development of the epitaxial growth process was supported by Microsoft Research. Portions of this work were conducted in the Minnesota Nano Center, which is supported by the National Science Foundation through the National Nano Coordinated Infrastructure Network (NNCI) under Award Number ECCS-1542202.

## Author contributions

M.G., G.G., and V.S.P. designed the differential resistance and conductance quantization experiments. G.G. fabricated and performed the transport measurements on Device 1 and 3 at UMN. M.G. fabricated and performed the transport measurements on Devices 2 and 3 at UMN. M.G. and G.G. analyzed the data on all devices under the supervision of V.S.P. M.P., J.D., and C.D. grew the heterostructure under the supervision of C.J.P. M.G wrote the numerical program for the RCSJ model calculations. M.G., G.G., and V.S.P. co-wrote the manuscript. All authors discussed the results and provided comments on the manuscript.

## Competing interests

The authors declare no competing interests.

## Additional information

**Supplementary information** The online version contains supplementary material available at https://doi.org/10.1038/s41467-022-33682-2.

**Correspondence** and requests for materials should be addressed to Vlad S. Pribiag.

**Peer review information** *Nature Communications* thanks the anonymous reviewer(s) for their contribution to the peer review of this work.

**Reprints and permission information** is available at http://www.nature.com/reprints

**Publisher's note** Springer Nature remains neutral with regard to jurisdictional claims in published maps and institutional affiliations.

**Open Access** This article is licensed under a Creative Commons Attribution 4.0 International License, which permits use, sharing, adaptation, distribution and reproduction in any medium or format, as long as you give appropriate credit to the original author(s) and the source, provide a link to the Creative Commons license, and indicate if changes were made. The images or other third party material in this article are included in the article's Creative Commons license, unless indicated otherwise in a credit line to the material. If material is not included in the article's Creative Commons license and your intended use is not permitted by statutory regulation or exceeds the permitted use, you will need to obtain permission directly from the copyright holder. To view a copy of this license, visit http://creativecommons.org/licenses/by/4.0/.

© The Author(s) 2022